

PAPER

Direct gyrokinetic comparison of pedestal transport in JET with carbon and ITER-like walls




To cite this article: D.R. Hatch *et al* 2019 *Nucl. Fusion* **59** 086056

View the [article online](#) for updates and enhancements.

You may also like

- [Experience on divertor fuel retention after two ITER-Like Wall campaigns](#)
K Heinola, A Widdowson, J Likonon et al.
- [Beryllium melting and erosion on the upper dump plates in JET during three ITER-like wall campaigns](#)
I. Jepu, G.F. Matthews, A. Widdowson et al.
- [The dependence of exhaust power components on edge gradients in JET-C and JET-ILW H-mode plasmas](#)
A R Field, C D Challis, J M Fontdecaba et al.

Direct gyrokinetic comparison of pedestal transport in JET with carbon and ITER-like walls

D.R. Hatch¹, M. Kotschenreuther¹, S.M. Mahajan¹, G. Merlo¹, A.R. Field², C. Giroud², J.C. Hillesheim², C.F. Maggi², C. Perez von Thun³, C.M. Roach², S. Saarelma² and JET Contributors^a

¹ Institute for Fusion Studies, University of Texas at Austin, Austin, TX 78712, United States of America

² CCFE, Culham Science Center, Abingdon OX14 3DB, United Kingdom of Great Britain and Northern Ireland

³ Forschungszentrum Jülich GmbH, Institut für Energie- und Klimaforschung–Plasmaphysik, 52425 Jülich, Germany

E-mail: drhatch@austin.utexas.edu

Received 26 February 2019, revised 25 April 2019

Accepted for publication 30 May 2019

Published 9 July 2019



Abstract

This paper compares the gyrokinetic instabilities and transport in two representative JET pedestals, one (pulse 78697) from the JET configuration with a carbon wall (C) and another (pulse 92432) from after the installation of JET's ITER-like Wall (ILW). The discharges were selected for a comparison of JET-ILW and JET-C discharges with good confinement at high current (3 MA, corresponding also to low ρ_*) and retain the distinguishing features of JET-C and JET-ILW, notably, decreased pedestal top temperature for JET-ILW. A comparison of the profiles and heating power reveals a stark qualitative difference between the discharges: the JET-ILW pulse (92432) requires twice the heating power, at a gas rate of $1.9 \times 10^{22} \text{ e s}^{-1}$, to sustain roughly half the temperature gradient of the JET-C pulse (78697), operated at zero gas rate. This points to heat transport as a central component of the dynamics limiting the JET-ILW pedestal and reinforces the following emerging JET-ILW pedestal transport paradigm, which is proposed for further examination by both theory and experiment. ILW conditions modify the density pedestal in ways that decrease the normalized pedestal density gradient a/L_n , often via an outward shift in relation to the temperature pedestal. This is attributable to some combination of direct metal wall effects and the need for increased fueling to mitigate tungsten contamination. The modification to the density profile increases $\eta = L_n/L_T$, thereby producing more robust ion temperature gradient (ITG) and electron temperature gradient driven instability. The decreased pedestal gradients for JET-ILW (92432) also result in a strongly reduced $E \times B$ shear rate, further enhancing the ion scale turbulence. Collectively, these effects limit the pedestal temperature and demand more heating power to achieve good pedestal performance. Our simulations, consistent with basic theoretical arguments, find higher ITG turbulence, stronger stiffness, and higher pedestal transport in the ILW plasma at lower ρ_* .

Keywords: pedestal, gyrokinetics, JET, transport

(Some figures may appear in colour only in the online journal)

^a See the author list of [71].

1. Introduction

This work studies the change in pedestal transport that arose due to the transition from the carbon (C) to ITER-like wall (ILW) on JET [1, 2]. The results help to explain the physics processes that increase pedestal transport in JET-ILW. The framework presented will, hopefully, be examined in more detail and built upon to optimize pedestal performance on JET-ILW and future experiments, like ITER, which may be subject to similar constraints.

The H-mode [3] pedestal drastically boosts confinement by supporting high temperatures at the plasma edge. These high temperatures can then propagate into the core where gradients are typically strongly limited by microinstabilities. Nearly all prospective burning plasma tokamaks, including ITER, have been designed to exploit an edge transport barrier. In order to achieve their aims, such devices will rely not only on the accessibility of an edge barrier but also on its robustness, measured, for example, by the attainable pedestal top temperature.

The properties of the H-mode pedestal are governed by three complex and sensitively interconnected components: (1) MHD stability, (2) SOL and divertor conditions (closely tied to wall materials, gas fueling, strike point location, pumping, etc), and (3) the transport (along with corresponding sources and sinks) from both neoclassical processes as well as residual micro-instabilities. In addition to their unique parameter dependences, these components collectively exhibit intricate co-dependences that have not been well-understood. It is, therefore, crucial to focus on parameter regimes that approximate as closely as possible reactor-relevant conditions simultaneously for all three components.

In this context, JET is at the forefront of this important aspect of fusion science due to its proximity to reactor conditions on two important fronts: its wall materials and its size (or more accurately, its dimensionless size, $\rho_* = \rho/a$, where ρ is the gyro radius and a is the minor radius). ITER will achieve values of ρ_* that are inaccessible in present day experiments and, due to its status as the largest operating present-day tokamak, JET can most closely approximate ITER's ρ_* regime. Moreover, since replacing C surfaces with a tungsten (W) divertor and beryllium (Be) first wall (i.e. the ILW), JET also serves as a laboratory for the effects of these wall materials.

Since beginning operation, JET-ILW has observed a degradation of confinement [4–11] attributable to a change in pedestal dynamics, including: a decrease in pedestal temperature; a trend toward progressively lower normalized confinement at progressively higher current and magnetic field; partial recovery of pedestal temperature and confinement with impurity seeding (in contrast to C operation where seeding degraded confinement); a demand for increased heating power to sustain high pedestal temperature; and stronger degradation of confinement than other metal wall devices [12]. Although much progress has been made on understanding and improving JET-ILW operation, the JET-ILW pedestal remains subject to significant constraints.

The residual pedestal transport is perhaps the least studied of the three components of the edge system. As we will argue in this paper, it may be the missing key for understanding many recent unexplained phenomena and optimizing operation in future devices. Transport, in combination with the relevant sources and sinks, determines the heating power necessary to achieve a given pedestal temperature; the inter-ELM evolution of pedestal density and temperature profiles, which ultimately determines the operating point at which an ELM is triggered; and the accessibility and properties of ELM-free regimes. An understanding of pedestal transport is an indispensable component of tokamak design and operation.

In this work we target an understanding of the transport dynamics governing the JET pedestal by studying, via linear and nonlinear global electromagnetic gyrokinetic simulations using the GENE code [13, 14], a pair of representative JET pedestals—one produced in recent ILW operation and an earlier one from C operation. The two discharges were selected to have good confinement ($H_{98} \sim 1$) at high current (3 MA) in order to study the pedestal dynamics and transport at low ρ_* . These two discharges have many comparable features but differ in the distinguishing characteristics of the transition from C to ILW, notably, significantly lower pedestal temperature for JET-ILW. In terms of operational parameters, the discharges differ in three important ways: (1) wall materials (W/Be, C), (2) fueling rates (1.9×10^{22} (e s⁻¹), 0), and (3) heating power (33 MW, 14.8 MW). Consequently, the subsequent analysis is an assessment of these combined effects on transport (note that (1) and (2) are tightly coupled due to the need to gas puff in JET-ILW in order to achieve W control in steady conditions).

The overarching goal is to identify various transport processes that pertain to and distinguish the pedestal dynamics of JET-C and JET-ILW. This work builds on previous studies of JET-ILW pedestal transport [15–17], which have demonstrated several connections between gyrokinetic simulations and experimental observations. Among other things, simulations in these works showed that ion scale turbulence can arise at low values of ρ_* because the velocity shear suppression is proportional to ρ_* . This can lead to the onset of major new transport mechanisms at low ρ_* . Hence, investigations of this question on JET is crucial to projecting to future burning plasmas.

We begin by briefly summarizing the major conclusions of this study. Our gyrokinetic analysis of the JET-C (78697) pedestal suggests that electron temperature gradient (ETG) driven modes and microtearing modes (MTM) are the major heat transport mechanisms. This is consistent with mounting evidence, spanning multiple machines [15, 18], that the observed fluctuations display the expected characteristics of these modes. This combination of transport mechanisms has also been proposed and analyzed in the context of inter-ELM transport and transport at the pedestal top [19–21]. Turning to the JET-ILW (92432) pedestal, we note that the distinctive features are lower temperature, shallower profile gradients, and higher $\eta = L_n/L_T$ ($L_{n,T}$ is the gradient scale length of the density, temperature, respectively). A major cause of these

changes is likely the effects of a metal wall on the density profile (both direct and indirect via the need for gas puffing) [22]. Often this change in the density profile is manifest as an outward shift [23], which effectively reduces the density gradient in the upper pedestal. Higher η translates into more robust ETG and ion temperature gradient (ITG) instabilities; demands additional heating power, and limits accessible pedestal top temperatures. Shallower gradients, particularly for the density profile, translate into weaker $E \times B$ shear, which, in combination with higher η , doubly exacerbates ITG turbulence. Remembering that the suppression of ion scale turbulence is deemed to be a principal mechanism for the pedestal formation, the unquenched ITG turbulence considered here for JET-ILW may be unique among present day machines. Higher values of η (i.e. high growth rates) and lower ρ_* (i.e. low shear rates) drive ITG turbulence, introduce new parameter dependences, including ρ_* and impurity content, which correlate with, and may cause, certain JET-ILW trends. This framework points to several plausible routes to optimizing pedestal performance, including control of radiation, neutral penetration (linked to particle sources), and SOL and pedestal density.

We note that ITG instability is sensitively dependent on the ion temperature profile, which is challenging to diagnose and remains subject to considerable uncertainty. Although we use a careful reconstruction of the ion temperature profile, the resulting predictions of ITG turbulence should be considered within the context of these uncertainties. Nonetheless, the regime examined in this ILW discharge approaches, perhaps more closely than any other presently accessible experiment, the conditions where such turbulence would be expected to arise in the pedestal (high η_i and low ρ_*). Consequently, the prediction of ITG pedestal turbulence should be carefully examined in an iterative process between experiment, simulation, and theory. Although many questions remain, this work, hopefully, lays the foundation for optimizing the transport and resulting confinement for JET-ILW and beyond.

This paper is organized as follows. Section 2 provides background information on pedestal transport and related research. Section 3 provides descriptions of the JET pulses. Section 4 describes the linear instabilities (both local and global) identified in gyrokinetic simulations. Section 5 describes the non-linear turbulence simulations and demonstrates agreement between simulated transport levels and a careful accounting of inter-ELM power balance. Section 5.2 describes the stiffness and ρ_* dependences expected from ITG pedestal turbulence, and section 5.5 discusses an ITG particle pinch. Section 6 provides a final discussion and summary.

2. Pedestal transport paradigm

The edge of an H-mode plasma is governed by at least three interconnected processes: (1) pedestal MHD stability, (2) divertor and SOL conditions, and (3) the residual transport (along with corresponding sources and sinks) in the edge transport barrier. Of these three, MHD stability is likely the best understood and is widely used to interpret and predict

pedestal structure [24, 25]. The pre-ELM pedestal pressure is typically observed to lie near the peeling ballooning stability boundary [24, 25], and ideal MHD has been successful at describing the ultimate pressure limit of the pedestal. There have been some notable exceptions for JET-ILW (see [7, 8, 26] for discussions of discrepancies with MHD limits and [27–29] for potential resolutions of these discrepancies).

Divertor and SOL conditions, which are closely tied to wall materials, gas fueling, strike point location, and pumping, also affect pedestal structure. The pedestal particle source and resulting density pedestal can be strongly affected by the SOL density, fueling levels, impurity content, and wall materials (metal walls having different reflection, retention, and outgassing properties) [22]. An effective outward shift of the density pedestal has also been observed in metal wall devices [22, 23, 30]. On AUG, for example, this has been attributed to the so-called high-field side high-density region. These various processes can impact both the MHD stability and the pedestal transport. In the context of the ILW, many of these processes act to reduce a/L_n in the pedestal (e.g. by raising the separatrix density), which has a very strong impact on the nature of microturbulence and its associated transport in the pedestal.

The residual transport in the pedestal arguably remains the least-understood component of the edge system and is the topic of this paper. Pedestal transport determines the inter-ELM trajectory of the density and temperature profiles in relation to the heating power and particle sources. This, in turn, determines the relative pedestal top temperature and density prior to the ELM crash. In this section, we briefly review an emerging paradigm for pedestal transport, the mechanisms involved, and their interplay with the other elements of the edge system (MHD and SOL). This paradigm is supported by the gyrokinetic results described below. Many of these topics are covered at a more fundamental level in [18].

Plasma profile evolution is governed by conservation laws (i.e. transport equations) for the temperature, density, and momentum of each species. These laws define the response of the profile to fluxes and sources, as illustrated, for example, in the continuity equation,

$$\frac{\partial n}{\partial t} + \nabla \cdot \Gamma = S_n, \quad (1)$$

where Γ is the particle flux and S_n is the particle source. The complete picture involves such equations for the density, temperature, and momentum of electrons, main ions, and impurity species. The focus of this work is on the most important subset of these channels, namely the density and temperature of electrons and main ions, which directly determine the confinement of energy. The relative sources for the different channels are controlled by very different mechanisms. The plasma temperature is maintained by outward flux from the core; particle sources include flux from NBI in the core, ionization of neutral particles from the edge and, possibly, a turbulent particle pinch [31, 32]; and impurities are drawn in from the edge by a neoclassical pinch. As may be expected from such different mechanisms, the drive for the different channels also varies widely in magnitude. A useful dimensionless metric for quantifying the drive of the various channels

is the ratios of their effective diffusivities (for example D/χ , where $D = \Gamma/\nabla n$, $\chi = Q/(n\nabla T)$). The use of effective diffusivities in this manner assumes neither the absence of pinches nor the absence of nonlocal effects, but is, rather, a convenient measure of the gradient that can be supported by a given flux or source. Alternatively, the parameter $S_n T/Q$ captures the relative drive of the two channels.

These relative drive quantities are difficult to determine experimentally but can be estimated by interpretive edge modeling. Such analyses have produced a consistent picture spanning multiple devices: the electron heat diffusivity far exceeds the particle diffusivity: $D/\chi_e \ll 1$ [32–34]—i.e. the heat source (flux from the core) far exceeds the particle source. Although such an analysis has not been carried out for the JET discharges examined here, it has been demonstrated via EDGE2D modeling of other JET-ILW pedestals [29].

Inter-ELM profile evolution also offers important information about the transport behavior. Pedestal profiles typically go through an early rebuilding period followed by a period of saturation that often makes up a substantial fraction of the inter-ELM cycle. In nearly all cases, the temperature experiences a pre-ELM period of saturation (or near-saturation) [20, 35–39]. The density evolution can exhibit more variation. On DIII-D and AUG, the density pedestal saturates early, often preceding the saturation of the temperature pedestal [37, 38]. On JET, the density often continues to evolve after the saturation of the temperature pedestal and in some cases the pedestal top density increases continuously until the ELM crash [20, 35, 39]. For the JET-ILW case of interest in this paper (92432), the temperature gradient becomes limited $\sim 30\%$ into the ELM cycle, while the density gradient becomes limited $\sim 50\%$ into the ELM cycle [39]. The pressure gradient is also fixed over the last half of the ELM cycle, roughly corresponding to the period of fixed density gradient. Both the pedestal top density and temperature increase gradually up to the ELM crash. The continued increase in temperature is likely due to the high heating power. Laggner *et al* [39] analyzes the inter-ELM profile evolution for this discharge as well as a wide range of other discharges spanning various heating and fueling conditions. Although the inter-ELM evolution can be complex, the pedestal top temperature generally appears to saturate prior to pedestal top density over a substantial range of conditions.

The contributors to pedestal transport must be consistent with the general picture outlined above. For example, each prospective transport mechanism has a distinctive transport *fingerprint* [18] defined by its relative impact on various transport channels. A minimum subset of pedestal transport mechanisms must include KBM (or similar MHD-like modes), ITG (or similar ion scale electrostatic modes), ETG, MTM, and neoclassical transport. MHD-like instabilities produce equal diffusivities in all channels. Consequently, such instabilities would fix the pressure profile at marginal stability and therefore preferentially impact the most weakly driven channel. Since the weakest (as quantified, for example, by a parameter like $S_n T/Q$) channel is typically the density, the impact of such modes would be limited to modifying the density gradients

via particle transport. ETG and MTM affect almost solely the electron heat channel and produce negligible particle transport. ITG (and other ion scale electrostatic modes like TEM) is more versatile, producing substantial ion (and some level of electron) heat transport and potentially producing inward, outward, or small (balanced pinch and diffusion) particle transport.

The transport mechanisms also have distinctive dependences on other parameters, like ρ_* . MTM and ETG have been found to be weakly affected by shear flow and exhibit scaling close to gyroBohm ρ_* dependence [16, 17]. ITG is typically thought to be suppressed by shear flow in the pedestal but may be excited by some combination of high growth rates and low shear rates (the relevant suppression parameter is $\gamma_{E \times B}/\gamma_{\text{lin}}$). Pedestal $E \times B$ shear rates are proportional to ρ_* and sensitively dependent on profile gradients due to the dominant neoclassical force balance in the pedestal (see section 5.2 for detailed discussion). Consequently, to the extent that JET-ILW is characterized by high η_i (high growth rates), weak density gradients (low shear), and low ρ_* (low shear), it resides in precisely the parameter regime where one might expect pedestal ITG turbulence to become important. Such was the conclusion of [16, 17], which observed a ρ_* threshold roughly corresponding to JET parameters below which ITG transport is not negligible. In agreement with basic theory, gyrokinetic simulations of pedestal ITG transport have identified the scaling $Q/Q_{\text{GB}} \propto \rho_*^{-2}$ [40], indicating a strong ρ_* dependence below this ρ_* threshold. We note that, while the focus of this paper is on ITG, the dynamics may translate to any ion-scale electrostatic mode like, for example, electron drift waves or trapped electron modes (TEM).

With this general information in hand, we are prepared to conceptually diagnose the limitations on the JET-ILW pedestal: (1) the main limitation for JET-ILW is low pedestal temperature; (2) JET-ILW demands additional heating power; (3) the pedestal top temperature generally saturates early in the ELM cycle; (4) heat diffusivities exceed particle diffusivities (not unique to JET-ILW). The culprit would seem to be a transport mechanism that preferentially produces heat transport and is amplified for JET-ILW. The following general picture emerges and is proposed for further study on JET-ILW. Metal walls modify the density profile via some combination of direct metal wall effects (e.g. different reflection/retention properties, or other effects on neutral penetration), the demand for gas puffing for W mitigation, or other SOL features like the high-field side high density region [22]. The net effect is a weaker density gradient, which increases $\eta = L_n/L_T$ [39] producing more robust ITG and ETG instabilities. These instabilities strongly limit the pedestal temperature and demand more heating power to achieve good pedestal performance. Crucially, both ITG and ETG preferentially produce heat flux over particle flux: ETG due to the absence of kinetic ions at electron scales, and ITG due to balanced pinch and diffusion (see section 5.5 for detailed discussion). The weak density gradient also decreases the flow shear rate, doubly affecting the ITG transport. The improved confinement with impurity seeding may be accounted for either directly (ion dilution

decreasing the turbulence) or indirectly (for example, seeding increasing pedestal particle sources or relieving the SOL conditions that weaken the density gradient).

At this point, two arguments against the above paradigm could be made. First, it might be supposed that a limitation on pedestal temperature could be compensated with an increase in pedestal density in order to maintain the same pressure and MHD stability properties. However, a limit on pedestal temperature does in fact have significant effects on the net confinement. A trade-off of temperature for density results in increased collisionality, generally resulting in less favorable MHD stability. For example, low pedestal temperature can feed back on MHD stability through collisionality and bootstrap current, pinning the pedestal in the unfavorable ballooning-limited regime and eliminating the advantages of shaping [8]. Aside from MHD stability, near the Greenwald limit, it is no longer possible to compensate a temperature deficit with higher density. Finally, with an eye toward a JET DT campaign, fusion gain is a very sensitive function of temperature (as opposed to pressure alone) in typical JET parameter regimes. Clearly, a limit on pedestal temperature has significant implications. A strong heat transport mechanism could also be related to slow inter-ELM recovery, discrepancies between ELM limits and peeling ballooning stability theory [7, 8], and transitions to type-III ELM regimes [41], although this must remain speculative as these topics have not been studied in this work.

The transport paradigm discussed here surely does not encompass all the effects limiting the JET-ILW pedestal. For example, studies examining the effects of SOL conditions or pedestal MHD stability (or both in combination) do explain some aspects of the observed metal wall behavior without appealing to any transport considerations [8, 9, 30, 42]. Moreover, further work is necessary to more firmly establish the hypothesis proposed in this paper. In particular, a detailed study of inter-ELM evolution could be conducted to understand how and when a weakened density gradient affects the transport and profile evolution. Moreover, uncertainties in the ion temperature profile and impurity content could be mitigated with further study. Nonetheless, the transport-oriented paradigm proposed here should become an integral part of the conceptual framework for understanding pedestal dynamics and should be actively probed by theory, computation, and experiment in future work.

In the context of these preliminary considerations, the next section describes two pedestals, JET-C (78697) and JET-ILW (92432), which will be examined within this framework.

3. Description of JET shots

Pedestal temperatures and normalized confinement times (relative to IPB98y2) are typically reduced in ILW plasmas relative to C, particularly at higher current and field [11], though the degradation of confinement is not universal in ILW plasmas and it can also be mitigated. JET pulse number 92432 was selected for this study since it represents a breakthrough in extending good confinement ($H_{98} = 1$) to higher current

Table 1. Summary of important parameters for JET pulses 78697 (C) and 92432 (ILW). I_p is the plasma current, B_T is the toroidal magnetic field, q_{95} is the safety factor at 95% of the minor radius (in terms of normalized poloidal magnetic flux), δ is triangularity, P_h is the total heating power, P_i is the inter-ELM power loss [44], Gas is the fueling rate, β_N is normalized plasma pressure, $T_{e,p}$ is the pedestal top electron temperature, and $n_{e,p}$ is the pedestal top electron density.

Pulse	I_p (MA)	B_T (T)	q_{95}	P_h (MW)	P_i (MW)
92432	3.0	2.8	3.0	33.0	11.6
78697	3.0	2.4	2.6	14.8	5.7
Pulse	δ	Gas (e s ⁻¹)	β_N	$T_{e,p}$ (keV)	$n_{e,p}$ (10 ¹⁹ m ⁻³)
92432	0.2	1.9×10^{22}	2.15	1.1	5.86
78697	0.24	0.0	1.8	1.68	4.19

(3 MA) and magnetic field (2.8 T) than was previously possible [43]. This is attributable to low fueling (lowest allowable for W control, albeit still substantial), high power to compensate for reduced pedestal temperature, and strike points located in the divertor corner for optimal pumping and density control [43]. An increased ratio of ion to electron temperature in the core also contributes to the improved confinement.

JET-C pulse number 78697 was also selected as a high current (3 MA) discharge with good confinement, and matches many of the relevant parameters of 92432 while retaining a higher pedestal temperature. It is important to keep in mind that, although these shots are representative in many ways, they clearly provide only a snapshot of the variation within and between each class of discharges. Important parameters are listed in table 1, which demonstrates the three main operational differences in the discharges, (1) wall materials, (2) fueling rate, and (3) heating power. Figure 1 shows the pedestal profiles of many of the important quantities. Notably, although the pedestal pressure is comparable between the two discharges, the total stored energy is higher in the JET-ILW pulse (8 MJ as compared to 6 MJ for the JET-C pulse) due to improved core confinement [43]. Temperature and density profiles are shown in figures 1(a) and (b). The main ion (deuterium) temperature is available for 92432 and shown in figure 1(a). The edge ion temperature is measured from the coupled CVI and NeX CX spectrum (the Ne comes from diagnostic puffs used to improve the quality of the CX data, given the very low C concentration in JET-ILW). The main ion species is then assumed to be thermally equilibrated with the impurities through collisional relaxation. This measurement is very challenging in the pedestal and subject to substantially uncertainty. For example, recent work on DIII-D exploiting a direct measurement of the main ions [45] has shown that the main ion temperature can deviate substantially from the impurity temperature in the pedestal sometimes resulting in a steeper gradient [46]. Ion temperature measurements are not available for 78697, for which we assume $T_i = T_e$ (this effectively places an upper bound on the role of ITG in 78697, which is found to be negligible). Figures 1(c)–(e) show several important quantities for the microinstabilities. The normalized density and temperature gradients (c) are much larger

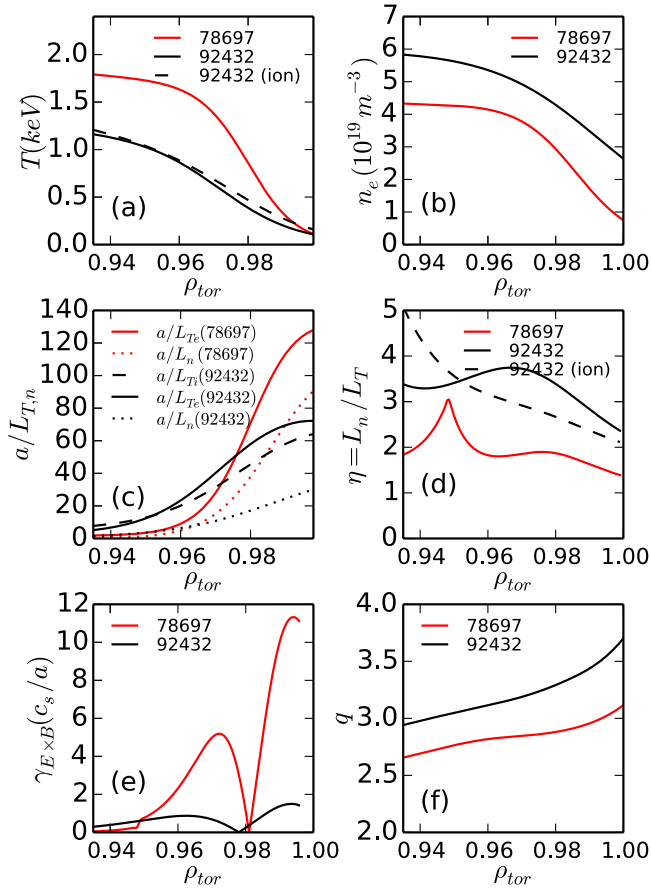


Figure 1. Profiles for JET-ILW (black) and JET-C (red) of temperature (a), density (b), a/L_n and a/L_T (c), $\eta = L_n/L_T$ (d), $E \times B$ shear rates (e), and safety factor q (f). Notably, JET-ILW has weaker gradients, higher η , and lower shear rates.

for JET-C (78697). This translates into much higher $E \times B$ shear rates (e) for JET-C (78697) due to the dominant neoclassical force balance between E_r and the profile gradients (see section 5.2 for a detailed description of the calculation of shear rates). Shear rates can also be affected by the toroidal rotation, which is reduced by gas puffing. Further work is needed to determine what combination of gas puffing and direct metal wall effects contribute to establishing the shear rate. Notably, η (d) is significantly larger for ILW (92432) than C (78697) due to a large decrease in density gradient on ILW (92432) (the large value of η is likely achieved by the much higher heating power in 92432). The q profile is shown in figure 1(f) and is less steep (i.e. lower magnetic shear) for JET-C (78697) due to the lower collisionality and higher bootstrap current. The inter-ELM profile evolution is described in section 2 and described more generally in [39]. Figure 1 will be referred to throughout the paper as the impact of these profiles on the relevant transport mechanisms is discussed.

From the information in table 1 and figure 1, one can quickly glean a striking difference in the transport between the two cases: the JET-ILW (92432) pedestal requires twice the heating power to achieve approximately half the temperature gradient and similar pedestal top pressure. To quantify this difference, the pedestal heat diffusivities are $\chi = Q/(n\nabla T) = 0.48 m^2 s^{-1}$

and $\chi = 0.12 m^2 s^{-1}$ for 92432 and 78697 respectively (quantities are taken in the middle of the steep gradient region of the pedestal). In these expressions, Q is the heat flux, n the electron density, T the electron temperature. From this quick comparison, one may suspect that a complete explanation of JET-ILW pedestal dynamics must include an understanding of these substantial differences in pedestal transport, which is the goal of this work. As described in the previous section, this paper proposes an emerging framework for the causes and manifestations of this change in transport. A more detailed understanding of the divertor, SOL, neutrals, materials considerations (etc) that cause the change in transport is equally important albeit outside the scope of this work.

4. Linear gyrokinetic analysis

We begin our gyrokinetic investigation with an examination of the underlying linear instabilities. Nonlinear simulations estimating the impact of these instabilities on the transport are described in section 5.

4.1. Local

The local flux tube approximation takes parameters at a single radial position, assumes constant gradients, and does not account for variation in background quantities. This can provide qualitative information but can also be misleading in systems where background quantities vary over relatively short radial scales. Critically, the local treatment knows nothing about the radial width over which a physics regime is operative—i.e. the effective ρ_* [47], which is determined by equilibrium variation over the steep gradient region. Despite these shortcomings, the local analysis provides valuable insights, makes connections with previous literature, and demonstrates qualitative differences between ILW and C. A more comprehensive global treatment is discussed in the next subsection.

Figure 2 shows growth rates and frequencies for JET-C (78697) and JET-ILW (92432) from local linear simulations in the middle of the steep gradient region of the pedestal ($\rho_{tor} = 0.98$). For both cases, KBM (black symbols) is observed at low k_y and electrostatic modes are observed at high k_y . For JET-C (78697), MTM is also observed at low k_y . The electrostatic instabilities at higher k_y have much higher growth rates for JET-ILW (92432), a trend that extends to ETG instabilities at electron scales (not shown). This local analysis involved scans of both binormal wavenumber k_y and ballooning angle (θ_0). The figure shows the maximum growth rate at each k_y . In the pedestal, the scan of ballooning angle is critical. Modes that are driven by toroidal resonances (i.e. resonances with the curvature and ∇B drifts), which is standard in the core plasma, peak at $\theta_0 = 0$. In contrast, due to the steep gradients in the pedestal, ω_* greatly exceeds the magnetic drift frequencies and slab resonances (with $v_{||}k_{||}$) can occur. This can produce modes with growth rates that have only weak dependence on, or even increase with, $|\theta_0|$. The MTM shown in figure 2, for example, are only the most unstable modes at

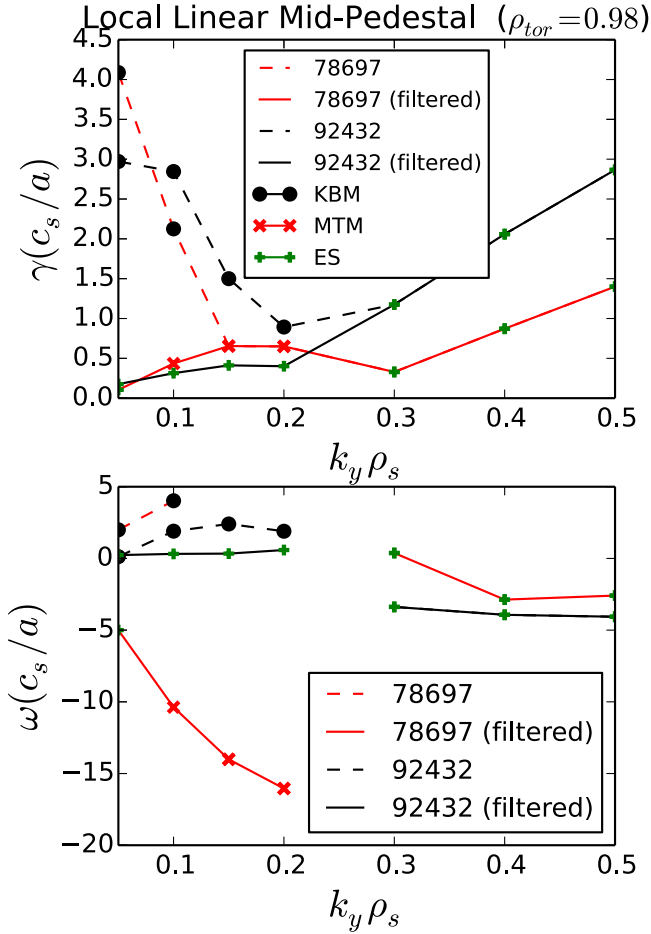


Figure 2. Growth rates (top) and frequencies (bottom) from local linear simulations (normalized to c_s/a of the corresponding discharge) in the steep gradient region for JET-ILW (92432) (black lines) and JET-C (78697) (red lines). Note that negative frequencies correspond to the electron diamagnetic direction. KBM, MTM, and electrostatic instabilities are observed. The KBM have very broad radial mode structures that are inconsistent with the width of the pedestal. The dashed lines, which find much closer agreement with global simulations, denote the instabilities that remain after filtering unphysically large radial modes.

$|\theta_0| > 0$. References [15, 17, 18] provide more discussion on this topic along with plots of the θ_0 dependence of growth rates.

The electrostatic modes and the MTMs will be discussed in more detail in the context of global simulations below (section 4.2). KBM, however, is not identified in the global simulations. We focus now on its potential role in these discharges.

A local description of strongly ballooning modes (i.e. modes peaked strongly at the outboard midplane) can be highly suspect in the pedestal, since such modes can have mode structures whose radial extent far exceeds the width of the pedestal. This consideration can be quantified by comparing the effective radial extent of the mode, as quantified by an eigenmode-weighted radial wavelength $1/\langle k_x \rangle$, with the width of the pedestal as encompassed in the following metric [18]:

$$\Theta = w \langle k_x \rangle, \quad (2)$$

where w is the width of the pedestal and $\langle k_x \rangle$ can be calculated from the linear eigenmode structure as

$$\langle k_x \rangle = \frac{\sum_{k_x} |k_x| |\phi|_{k_x}^2}{\sum_{k_x} |\phi|_{k_x}^2}, \quad (3)$$

so that a mode that is strongly peaked at the outboard mid-plane ($k_x = 0$) has a very low value of Θ . Flux tube simulations with GENE include several k_x modes (each having a parallel domain spanning $z = (-\pi, \pi)$) connected with the flux tube parallel boundary condition [48]. The ballooning angle $\theta_0 = \frac{k_{x,center}}{\hat{s}k_y}$ (i.e. the central k_x value) can be chosen for each linear flux tube simulation and the remaining k_x values, $\Delta k_x = 2\pi \hat{s}k_y$, are defined by the parallel boundary condition. The connected k_x modes constitute the extended ballooning structure of the mode so that the sum over k_x defined in equation (3) weights each $z = (-\pi, \pi)$ segment with its corresponding value of k_x . The criterion $\Theta > 2$ indicates whether a mode predicted by local theory plausibly fits within the radial range over which it is driven. If this criterion were to hold, it would indicate whether the local mode could in principle be physical (i.e. whether the local mode can be captured by a higher fidelity global treatment of the system). The KBM modes corresponding to figure 2 do not satisfy this criterion and, consequently, are not observed in the global simulations described below.

Several studies examining KBM stability in the pedestal yield widely varying conclusions: KBM is unstable, albeit close to marginal [19]; KBM is locally stable in most of the pedestal owing to the bootstrap current giving access to 2nd stability [20]; KBM is unstable [36]; KBM is unstable but subdominant to electrostatic modes [49]; KBM is stable but near the instability threshold when β is artificially increased [50]; KBM is stable and remains stable when self-consistently varying the equilibrium consistent with increasing pressure gradients (i.e. KBM is in a second stability regime) [51]; KBM is in a second stability regime locally, which disappears in a global treatment [52]; KBM is in second stability in both local and global analysis when self consistently increasing pressure gradients with equilibrium [15].

In the context of this study we can make the following statements about pedestal modes: (1) KBM is identified in local simulations but has mode structures inconsistent with the narrow width of the pedestal and is not found in our global treatment, and (2) In the magnetic fluctuation data available for JET, one can identify fluctuations that appear to correspond closely with MTM and eliminate KBM on the basis of simple frequency comparisons. In spite of these considerations, KBM (or some similar MHD activity) cannot be ruled out because it may be only marginally unstable and due to several other considerations, including uncertainties in input data, the limited fluctuation diagnostics available, and limitations of pedestal gyrokinetics for low- n MHD. Regarding the latter, a rigorous MHD analysis would include the vacuum solution and the kink drive term, both of which are planned for future work. Perhaps the best evidence of some sort of KBM-like MHD behavior is its apparent utility (or the utility

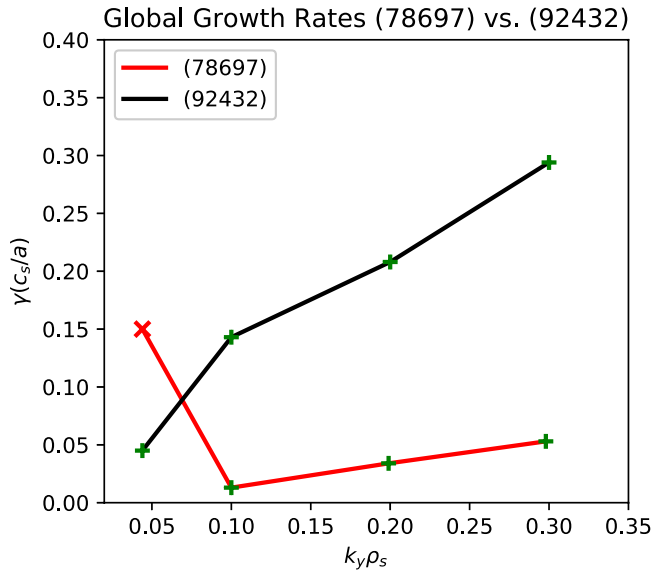


Figure 3. Growth rates from global simulations (normalized to mid-pedestal c_s/a of the corresponding discharge) for JET-ILW (92432) (black line) and JET-C (78697) (red line). The instabilities are ITG modes, with the exception of the lowest k_y JET-C (78697) mode, which is an MTM.

of its proxy relation between β and pedestal width) in the EPED model and the observation that inter-ELM profile evolution often allows separate density and temperature changes constrained by a fixed pressure profile (see, for example, [39, 50]). In any case, the transport fingerprint of KBM [18] eliminates it as a major heat transport mechanism due to its large ratio of D_e/χ_e . It can therefore be ruled out as the mechanism limiting the pedestal temperature in JET-ILW and is not of primary interest in this work.

4.2. Global

Having briefly surveyed the local linear gyrokinetic stability picture, we turn now to a global treatment, which accounts for the strong profile variation over the narrow pedestal. Background rotation (described in more detail in section 5.2) is included in these global linear simulations (in contrast with the local simulations in which background shear produces Floquet modes). Global k_y scans comparing ILW (92432) and C (78697) are shown in figure 3 where green symbols denote electrostatic (ITG) modes and the red x denotes a MTM observed at low k_y in the JET-C (78697) pedestal. This MTM occurs at toroidal mode number $n = 8$, at which a magnetic fluctuation can be observed in magnetic spectrograms for this discharge (this will be described in detail in a future paper). The large difference in η for JET-C (78697) and JET-ILW (92432) is reflected in a corresponding difference in ITG growth rates. This is further enhanced by the much larger JET-C (78697) shear rate (see figure 1(e)), suggesting that the ion scale ITG transport for JET-ILW (92432) is expected to be much higher than that of JET-C (78697).

The nature of the instabilities is explored in figures 4 and 5, which show several parameter variations for $k_y \rho_s = 0.2$ whose dependences are consistent with ITG and MTM. All parameter

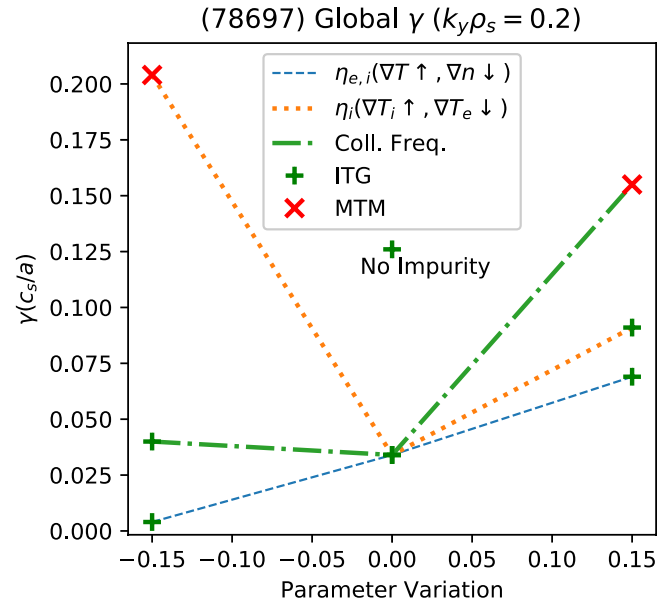


Figure 4. Parameter sensitivities from global simulations at $k_y \rho_s = 0.2$ for JET-C (78697). The x-axis denotes the fractional change ($\pm 15\%$) in various parameters (annotated in the figure). All parameter variations are constructed to keep the pressure fixed (e.g. the annotation $\eta_i(\nabla T_i \uparrow, \nabla T_e \downarrow)$ denotes an increase in η_i that keeps pressure fixed by increasing the ITG and decreasing the electron temperature gradient). The instability found with nominal inputs has the parameter dependences of an ITG mode. An MTM becomes dominant with minor increases in collision frequency and electron temperature gradient. Sensitivity to impurities is demonstrated by the large increase in growth rate (labeled No Impurity) observed when C is not included.

variations are constructed to hold pressure fixed (e.g. increases in temperature gradient are compensated by decreases in density gradient, etc) and thus avoid decoupling profile effects from equilibrium effects in an inconsistent manner. Growth rates of the electrostatic modes increase with ITG and temperature ratio T_e/T_i and are insensitive to collision frequency. MTMs arise in these scans for the JET-C (78697) pedestal as the collision frequency or electron temperature gradient is increased. As seen in figure 3, the JET-C (78697) pedestal lies above the MTM threshold for other k_y , suggesting that MTM play an important role in this JET-C (78697) pedestal. A detailed analysis of the MTM in 78697 will be presented in a future paper.

The ILW simulations include a dynamic Be impurity at the level of $Z_{\text{eff}} = 1.8$ and the C simulations include a dynamic C impurity with $Z_{\text{eff}} = 2.35$. The Z_{eff} estimate is derived from a line averaged measurement from visible Bremsstrahlung, which provides no profile information (constant Z_{eff} is thus assumed). The impurity content is subject to considerable uncertainties. For example, for JET-ILW (92432) the diagnosed value of Z_{eff} is produced by some mixture of impurities, including Be and Ni, but the precise densities are unknown. The instabilities can be highly sensitive to the impurity content; as shown in figure 5 the ITG growth rate increases by $\sim 65\%$ when ion dilution is neglected (i.e. no impurity is included, or alternatively assuming the Z_{eff} is attributable mostly to high Z Ni), and decreases by $\sim 40\%$ when the impurity gradient

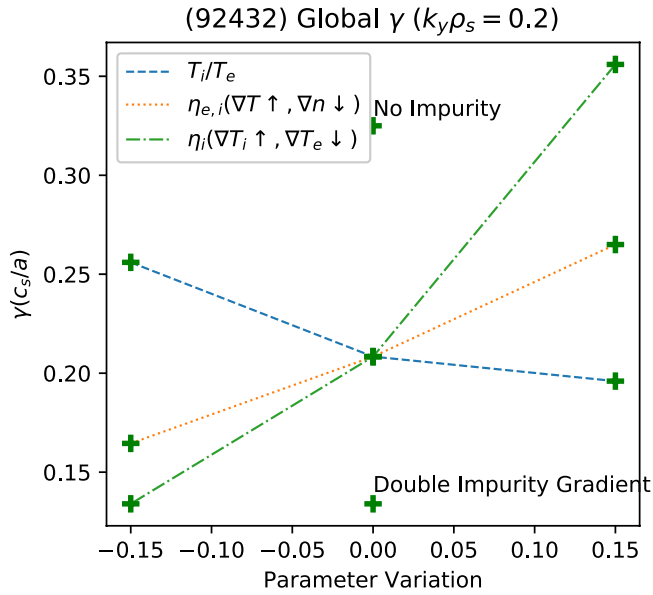


Figure 5. Parameter sensitivities from global simulations at $k_y \rho_s = 0.2$ for JET-ILW (92432). The x -axis denotes the fractional change ($\pm 15\%$) in various parameters (annotated in the figure). All parameter variations are constructed to keep the pressure fixed (e.g. the annotation $\eta_i(\nabla T_i \uparrow, \nabla T_e \downarrow)$ denotes an increase in η_i that keeps pressure fixed by increasing the ITG and decreasing the electron temperature gradient). The instability clearly exhibits the expected parameter dependences of an ITG mode. Sensitivity to impurities is demonstrated by the large increase in growth rate (labeled No Impurity) observed when Be is not included.

is doubled. Likewise, the ITG growth rate in JET-C (78697) increases by a factor of four when C is neglected, as seen in figure 4. This reinforces similar observations in [16, 17] and is consistent with the beneficial effects of impurity seeding in the ILW pedestal.

Notably, KBM is not observed in the global simulations, consistent with the criterion described above for local simulations. Scans of β were undertaken in order to probe proximity to the KBM limit and more generally to determine the sensitivity of the various modes to electromagnetic effects. As shown in figure 6, in this global treatment an artificial (i.e. not self-consistently modifying the background equilibrium) $\sim 40\%$ increase in β produces KBM instability in both the JET-ILW (92432) and JET-C (78697) pedestals for this wavenumber.

In addition to the high β KBM limit, a low β threshold is also observed below which an electron drift wave becomes dominant. This electron drift wave is excited by a parallel resonance and is suppressed by electromagnetic effects. In the intermediate range, the slab ITG mode is very insensitive to β . This suggests that, while certain pedestal modes are completely electrostatic in nature, it is necessary to include some level of electromagnetic effects in order to suppress spurious (i.e. only unstable at β values far below the experimental values) electrostatic modes.

5. Nonlinear simulations

Having characterized the linear instabilities identified in the JET-C (78697) and JET-ILW (92432) pedestals, we turn now

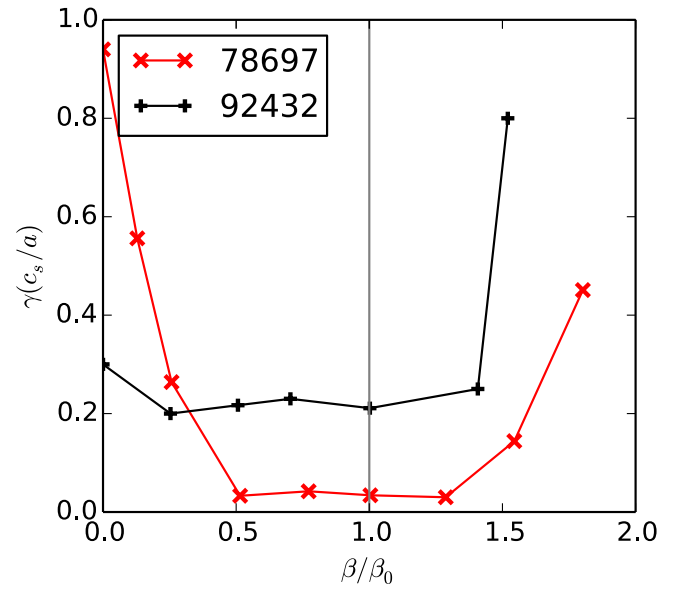


Figure 6. Growth rates from global simulations scanning β (not accounting for self-consistent variation of the equilibrium) at $k_y \rho_s = 0.2$ for JET-ILW (92432) (black) and JET-C (78697) (red) demonstrating the insensitivity of the slab ITG modes to β . However, some level of electromagnetic effects are important to suppress a highly unstable electrostatic mode that is manifest at low β . The profiles lie $\sim 40\%$ below a KBM limit, indicated by the sharp rise at higher β .

to the nonlinear simulations that are necessary to quantify how these instabilities are manifest in the transport. We employ a flux tube approximation for the small scale ETG turbulence and a global approach for the ion scale turbulence. Although cross-scale interaction can not be ruled out, fully self-consistent multiscale simulations must await a large dedicated computer allocation. Local neoclassical simulations are also carried out with GENE [53]. Detailed information about the simulations for these various modes of operation is provided in appendix.

As will be described below, simulations find close agreement (except near the separatrix) with carefully diagnosed [44] inter-ELM heat flux levels. Such agreement is by no means a foregone conclusion and adds credence to the conclusions of this paper. Several elements are necessary to achieve such realistic transport levels. (1) Although the ITG turbulence described below is electrostatic and insensitive to β , some level of electromagnetic effects (i.e. finite β) is necessary to suppress the low β electron drift waves that would otherwise dominate (see discussion surrounding figure 6). For other instabilities, like MTM and KBM, full electromagnetic effects (i.e. the precise experimental value of β) would be required. (2) A global treatment is necessary to capture the limited domain of the steep gradient region. This eliminates the large radial structures that dominate local pedestal flux tube simulations and produce unrealistically large transport levels. The mechanism is closely related to those described, e.g. in [47, 54]. (3) A global treatment is additionally necessary to quantitatively capture the effects of the radial variation of geometry, magnetic shear, and profiles. In our experience the limited radial domain (2) is an absolute necessity, whereas

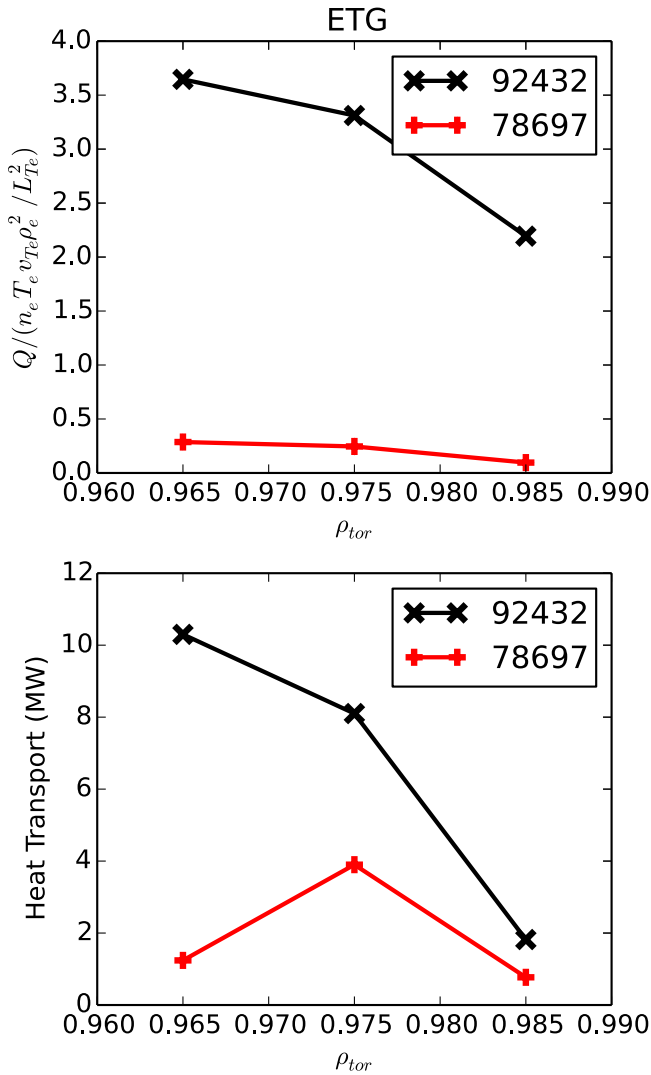


Figure 7. Heat fluxes (top) from local flux tube single scale ETG simulations for JET-ILW (92432) (black) and JET-C (78697) (red) normalized to electron gyroBohm units (including the electron temperature gradient scale length). As expected from the profiles (notably higher η), JET-ILW (92432) produces substantially higher heat fluxes, although the difference is decreased in the un-normalized quantities (bottom). These simulations suggest that ETG produces experimentally relevant transport levels in both discharges (for reference the inter-ELM power is 11.6 MW and 5.7 MW for ILW and C, respectively).

many semi-quantitative features can be captured with a local treatment that enforces a limited radial domain (with Dirichlet boundary conditions) corresponding to the pedestal width, as described in [15, 16].

5.1. ETG turbulence: comparison of JET-ILW and JET-C

Due to its small spatial scales, ETG turbulence is amenable to nonlinear local flux tube simulations, which are described in this subsection. ETG simulations are sensitive to not only temperature and density gradients, but also the temperature ratio and Z_{eff} , all of which are taken directly from the best available experimental estimates. In agreement with earlier work [15, 50, 55, 56], the pedestal ETG turbulence described

here is slab-like and isotropic, in contrast with the streamer-dominated core ETG turbulence.

Consistent with the large difference in pedestal η_e , JET-ILW (92432) produces order of magnitude larger gyroBohm-normalized ETG heat fluxes than JET-C (78697), as shown in figure 7 (top) for three points in the pedestal. The electron gyroBohm normalization [50] using the electron thermal velocity, electron gyroradius, and electron temperature gradient scale lengths appears to be very appropriate, as it produces (roughly) order-unity fluxes. As noted, for example, in [16, 17, 57], ETG is sensitively dependent on Z_{eff} , which tends to be lower in JET-ILW than JET-C and would improve with increased Z_{eff} associated with impurity seeding.

Although the normalized quantities differ by an order of magnitude, the raw heat transport is much more comparable between the two cases, as shown in figure 7 (bottom), which shows the ETG heat transport in units of MW. Notably, as a fraction of the total heat flux, the ETG transport is roughly equal for JET-ILW (92432) and JET-C (78697) (recall that the inter-ELM power losses are approximately twice as large for 92432—see table 1). The fact that, despite widely varying gradients and gyroBohm fluxes, the two systems produce transport levels comparable to the experiment strongly suggests that ETG is an important transport mechanism in the JET pedestal.

5.2. ITG turbulence in the JET-ILW pedestal

In this section we describe the ion scale ITG turbulence, which may be the transport mechanism that is most distinctive to JET-ILW and responsible for its differences from standard pedestal regimes (JET-C and other experiments). Although ITG turbulence is the major ion-scale instability in this JET-ILW discharge (92432), many of the dynamics may apply to other ion scale electrostatic modes like electron drift waves and TEM. Within the framework described in section 2, such turbulence is likely robustly suppressed in both JET-C and other experiments (metal wall and otherwise). For smaller experiments (i.e. higher ρ_*), ion scale transport is typically suppressed by the correspondingly stronger $E \times B$ shear rates. Whereas for JET-C, such turbulence is likely suppressed due to some combination of reduced η , stronger shear rates (due to steep gradients), and stronger ion dilution from C impurities.

The ITG turbulence described below is similar to that investigated in detail in [16, 17, 40]: slab-like ITG turbulence that closely follows basic theoretical predictions for its response to shear flow [40]. In some simulations, β was reduced (up to 40%) in order to avoid numerical instabilities. Linear and non-linear simulations verified that this reduction did not change the properties of the transport, since the slab ITG turbulence is insensitive to β (see, e.g. figure 6). Further details are provided in appendix. Simulations with beta values close to the ideal ballooning threshold tend to be very challenging and will be published elsewhere, highlighting the capabilities of some of GENE's newly developed numerical schemes for treating high-beta regimes. Simulations span from just inside the pedestal top to near the separatrix ($\rho_{\text{tor}} = 0.94$ –0.995,

closely corresponding to the range shown in figure 1) with narrow regions at each end dedicated to a buffer zone where gradients are smoothly flattened and fluctuations are gradually set to zero (see appendix for simulation details).

In order to realistically model the turbulence, the flow shear must be properly accounted for. Direct measurements of the radial electric field E_r and parallel flow $V_{||}$ were not available for this discharge. Consequently, we estimate E_r using the standard neoclassical formula [58],

$$V_{||} = -\frac{RB_\phi}{ZeB} \left(\frac{1}{n_i} \frac{dP_i}{d\psi} + Ze \frac{d\Phi_0}{d\psi} - k_{||} \frac{B^2}{\langle B \rangle^2} \frac{dT_i}{d\psi} \right) \quad (4)$$

where $V_{||}$ is the parallel flow, R is major radius, B_ϕ is the toroidal magnetic field, P_i is ion pressure, Φ_0 is the electrostatic potential, and ψ is the normalized poloidal magnetic flux (readers are referred to [58] for more detailed definitions, e.g. of $k_{||}$). Since there is no measurement available, we use the approximation $V_{||} = 0$, which is justified by the experimental observation [59] that in the pedestal the dominant balance in equation (4) is between the radial electric field and the gradients. Note that the Doppler shift in the pedestal is in the electron diamagnetic direction and thus opposite to that of the bulk plasma rotation in the core, so the inclusion of $V_{||}$ would be expected to slightly decrease the net Doppler shift. We have calculated the effect of $V_{||}$ for similar JET-ILW discharges and find that it reduces the Doppler shift by a few ten percent (varying widely over the pedestal) and reduces the shear rate by 0%–15%—i.e. it would produce a quantitative but not qualitative change in the turbulence. Note that the final term on the RHS of equation (4) reduces the impact of the ITG so that the density gradient is particularly impactful on the radial electric field.

The shear rate used in GENE is a flux function defined as

$$\gamma_{\text{GENE}} = \frac{\rho_{\text{tor}}}{q} \frac{d}{d\rho_{\text{tor}}} \frac{E_r}{B_\theta R}, \quad (5)$$

where ρ_{tor} is the square root of the normalized toroidal flux. For global GENE simulations, the shear rate varies radially over the box and includes a region of zero shear as seen in figure 1(e) (see [40] for a detailed discussion of pedestal $E \times B$ shear).

Figure 8 shows the resulting heat transport for several variations of the simulations inputs. The first two columns probe sensitivity to impurities by exploring the two limiting assumptions for impurity content: first, that the diagnosed value of Z_{eff} is fully attributable to beryllium (i.e. maximum ion dilution), which is the material of the first wall, and second, that it is attributable to fully stripped nickel (i.e. minimal ion dilution). Both treatments produce experimentally relevant transport levels. The high sensitivity to ion dilution is demonstrated by the nearly three times increase in transport for the low dilution assumption. The precise impurity mixture cannot be precisely determined experimentally, so that the most realistic transport estimate is expected to lie somewhere between these two bounds. The third column in figure 8 demonstrates sensitivity to the ITG via a simulation using $T_i = T_e$, effectively increasing the ITG by an average of 19% over the pedestal

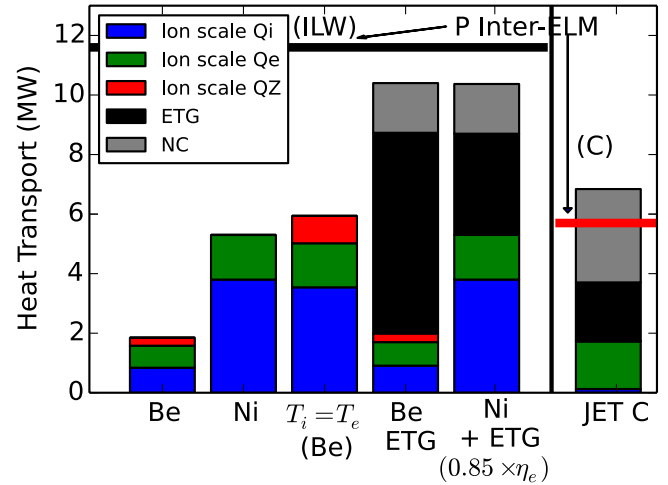


Figure 8. Contribution to heat transport from global simulations of JET-ILW (92432) (first three bars), combined with ETG and neoclassical (bars four and five). The first two columns probe sensitivity to ion dilution by using $Z_{\text{eff}} = 1.8$ and two bounding assumptions for the impurity makeup: entirely beryllium (high dilution) and entirely nickel (low dilution). The comparison of the third column ($T_i = T_e$) with the first column (T_i from charge exchange, which estimates a $\sim 20\%$ decrease in a/L_T) tests sensitivity to the ion temperature gradient. The fourth and fifth columns demonstrate two possible routes to reproducing the total power balance by combining transport from single scale ETG simulations and neoclassical simulations with global ion scale simulations. The fourth column uses beryllium and the fifth column uses nickel along with a 15% reduction in η_e for the ETG simulations. The last column shows transport from JET-C (78697) simulations (note the absence of turbulent ion heat flux).

([46] suggests that main ITG may be larger than those inferred from impurity temperatures). These simulations suggest that ion scale ITG turbulence (1) contributes experimentally relevant levels of transport, (2) is sensitive to impurity content, and (3) limits the ITG and by extension the pedestal top temperature.

The fourth (Be) and fifth (Ni) columns in figure 8 show the sum of ion scale ITG transport, single scale ETG transport (with nominal profiles fourth and a 15% reduction in η_e fifth), and neoclassical transport, demonstrating two plausible combinations that recover power balance. The ETG and neoclassical transport are averaged over three points in the pedestal ($\rho_{\text{tor}} = 0.965, 0.975, 0.985$), and the global ion scale transport is taken to be the average from $\rho_{\text{tor}} = 0.96$ – 0.99 . The radial dependence of the fluxes is shown in figure 9. For all transport channels, the fluxes decrease toward the outer region of the pedestal. The total transport closely matches power balance in the mid and upper pedestal but underpredicts near the separatrix. The discrepancy may be due to sensitivities to uncertain inputs (profile fits, impurity content, etc), or alternatively an additional transport mechanism (e.g. blobs) that depends intrinsically on cross-separatrix dynamics. The estimated inter-ELM power loss (11.6 MW) is also shown in figures 8 and 9. Estimating this inter-ELM power loss,

$$P_{\text{sep}} = P_{\text{abs}} - P_{\text{rad}} - \frac{dW}{dt}, \quad (6)$$

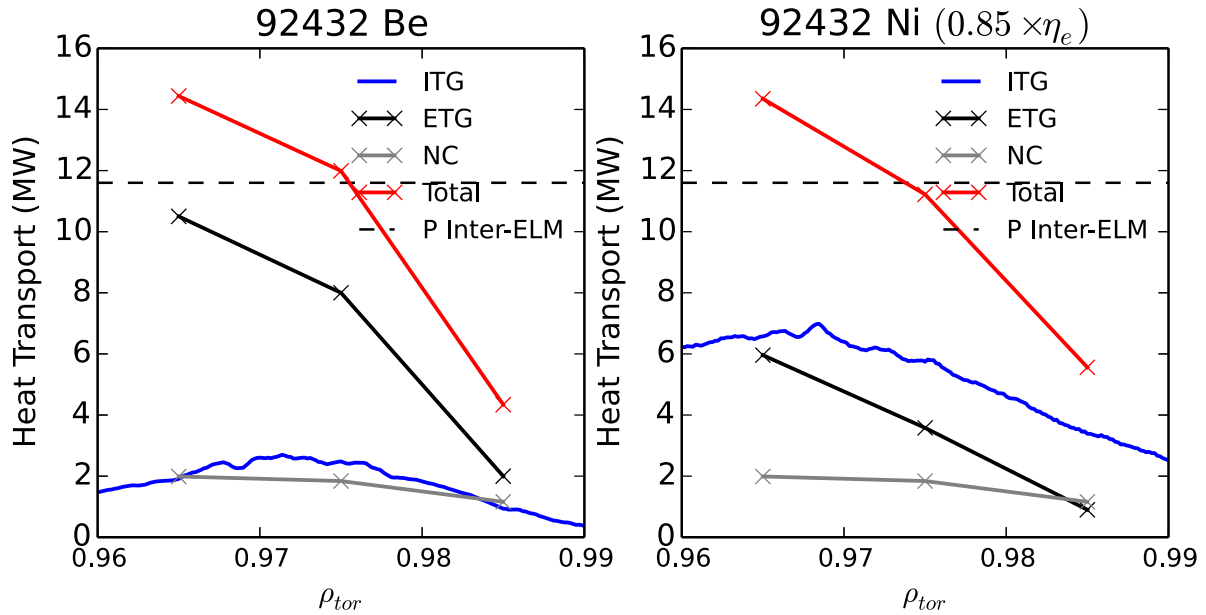


Figure 9. Radial dependence of heat transport for 92432 using Be (left) and Ni (right). The simulations match power balance closely at mid and upper pedestal but underpredict heat transport near the separatrix. The discrepancy may be due to sensitivities to uncertain inputs (profile fits, impurity content, etc), or alternatively an additional transport mechanism (e.g. blobs) that depends intrinsically on cross-separatrix dynamics.

involves a careful accounting of the radiation from the confined plasma (P_{rad}), time-averaged ELM losses (dW/dt , corresponding also to the inter-ELM buildup of the pedestal), and total absorbed heating power (P_{abs}) [44]. For 92432, the pressure increases continuously at approximately a constant rate during the ELM cycle [39] so that the inter-ELM dW/dt must be accounted for (the profiles are averaged over the last 20% of the ELM cycle). The time-averaged ELM loss power and the radiated power each account for about a third of the total loss power. Hence, the transport loss power between ELMs is substantially lower than the total power absorbed.

5.3. Ion scale turbulence in JET-C

Global ion scale simulations for JET-C (78697) proved challenging due to two factors. First, at realistic values of β , simulations either encountered numerical instabilities or (possibly related) proved extremely challenging due to the presence of MTM at low k_y . Second, low β simulations seeking to avoid these challenges were polluted by the spurious electrostatic electron drift waves that are suppressed by electromagnetic effects (described in section 4, see figure 6). Stable simulations were achieved via a combined reduction of β (by a factor of four) and the electron temperature gradient (by 30%). These changes served the intended purpose of suppressing numerical instabilities, MTM, and the low β electron drift wave while leaving the ITG growth rates unchanged. The resulting transport, shown in the last column of figure 8, is composed almost entirely of electron heat flux, demonstrating the full suppression of ITG turbulence. A substantial fraction of the heat flux is electromagnetic, suggesting that some MTM activity persists even at this low value of β . Due to the substantial parameter modifications, which, in particular, affect the MTM instabilities, this simulation should

not be considered a high-fidelity reproduction of the pedestal turbulence. Nonetheless, it is sufficient to demonstrate the full suppression of ITG fluctuations in contrast with the JET-ILW (92432) pedestal described above. This suppression was to be expected in light of the low ITG growth rates (figure 3) and high shear rates (figure 1(e)) for 78697.

5.4. Stiffness and shear rate scaling

Typically ion heat flux in the pedestal is thought to be reduced to near-neoclassical levels [60, 61]. This is consistent with the JET-C (78697) simulations described above. In contrast, the JET-ILW (92432) simulations described above predict that neoclassical transport produces only between 30%–70% of the ion heat flux (note that ETG remains a major, possibly dominant, transport mechanism). Notably, consistent with the present study, a separate dedicated study of neoclassical transport for JET-ILW concludes that the neoclassical ion heat flux is low and unlikely to account for the experimental ion heat flux [29].

Since neoclassical processes have generally been thought to account for pedestal ion heat flux, the addition of ITG turbulence would represent a qualitative change with respect to conventional pedestal regimes. One implication is a substantial increase in stiffness (i.e. response of flux to gradients). This is demonstrated in figure 10, which shows the relative stiffness of ETG, ITG, and neoclassical heat transport. In contrast with neoclassical transport, ETG and ITG turbulence exhibit a high degree of stiffness. Note that this high gradient ITG simulation shown in figure 10 does not account for the increase in $E \times B$ shear, which decrease to some degree the observed stiffness.

The addition of ITG transport will also introduce a new ρ_* sensitivity via the dependence of ITG transport on $E \times B$ shear rates. Previous gyrokinetic studies have found that

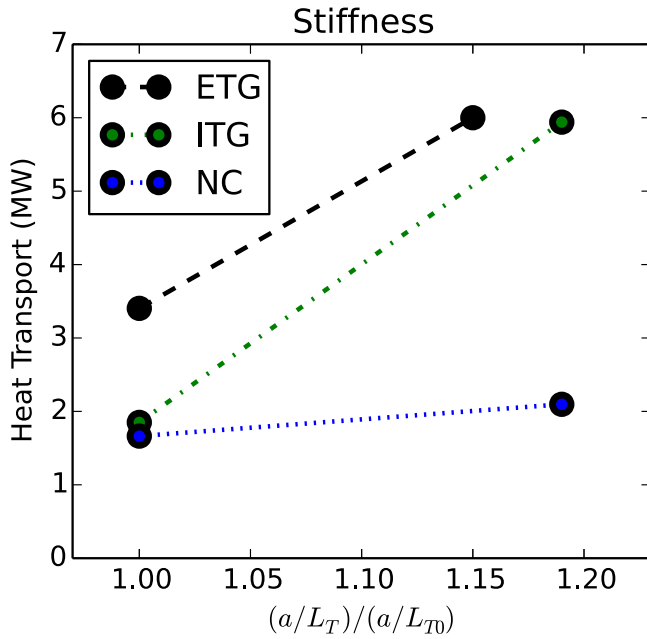


Figure 10. Stiffness (i.e. response of transport to driving gradients) of ETG, ITG, and neoclassical transport for 92432 (Be). The ITG transport is extremely stiff in comparison with neoclassical, indicating the increased stiffness expected in pedestal regimes involving non-negligible ITG transport.

MTM, ETG, and neoclassical transport in the pedestal closely follow gyroBohm ρ_* scaling ($Q \propto \rho_*^2$), which in turn closely follows empirical scaling laws [16, 17]. In these studies, pedestal ITG, on the other hand, was found to be strongly shear suppressed at high ρ_* but exhibited a very unfavorable ρ_* scaling, becoming non-negligible in the regimes of relevance for JET-ILW (low shear, high growth rates).

Hatch *et al* [40] examines in detail this scaling of pedestal ITG transport on ρ_* and $E \times B$ shear. Since the pedestal ITG turbulence is slab like, many recent shear suppression models, which are oriented around the core-relevant toroidal picture, are less applicable and early slab decorrelation theories become highly relevant. In particular, the decorrelation theory described in [62, 63] finds excellent agreement with simulations and predicts the scaling $Q/Q_{GB} \propto \gamma_{E \times B}^{-2}$. The ITG turbulence studied here also finds good agreement with this scaling as seen in figure 11, which shows $Q/Q_{GB} \propto \gamma_{E \times B}^{-1.7}$ for the ion heat flux channel, and $Q/Q_{GB} \propto \gamma_{E \times B}^{-1.55}$ for the total ion scale transport. We emphasize that this scaling applies only to the ITG component of the transport. The total transport typically has large contributions from gyroBohm mechanisms like ETG, MTM, and neoclassical. Such was the case described in [16], where gyrokinetic simulations reproduced experimentally identified ρ_* scaling [64] above a certain threshold in ρ_* .

To put the ρ_* scaling in context, the ITG transport would be up to six times stronger for JET than for a system matching other dimensionless parameters and pedestal gradients on DIII-D or AUG (assuming a factor of three difference in ρ_*). Likewise, within JET operational bounds, a factor of ~ 2 difference in ITG transport could be expected (assuming a factor of ~ 1.5 variation in ρ_* [65]). The scaling could be even more

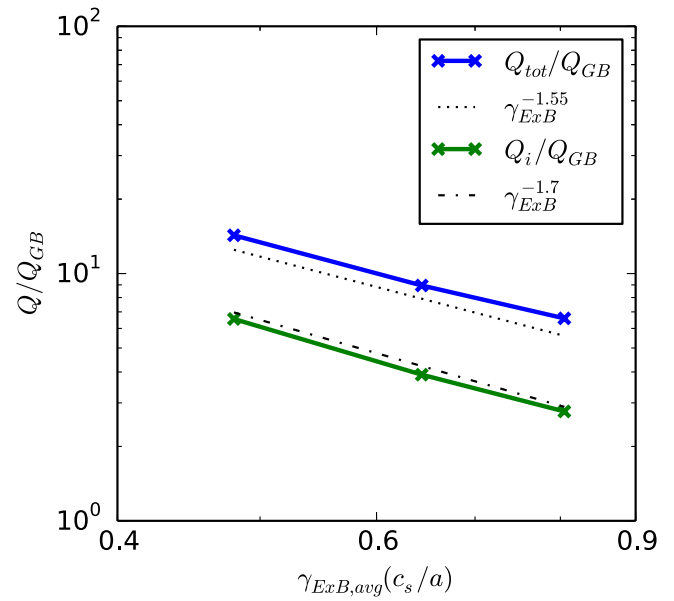


Figure 11. Heat flux from nonlinear global simulations of ITG turbulence for JET-ILW (92432) scanning $E \times B$ shear rate. Both the ion heat flux (green) and total heat flux (blue) are shown. The scaling is consistent with predictions from basic theory [40] and suggests high sensitivity to ρ_* . Note that the total heat transport (including, e.g. ETG) would have a much weaker scaling.

severe if pedestal growth rates are enhanced at low ρ_* , e.g. by changes to the density profile in connection with more stringent operational constraints necessary to mitigate more energetic ELMs. These dynamics are plausible contributing factors to both the more-severe confinement degradation (at least early in JET-ILW operation) due to metal walls on JET than AUG [12] and the degradation on JET at low ρ_* . Moreover, although no rigorous predictions can be made, these trends may portend a fundamental regime change for the ITER pedestal [17]. Notably, such a change has also been described in [66], where the decrease in shear rate was found to result in streamers near the separatrix that broaden the SOL width. Successful sustainment of the ITER pedestal may require pedestal profile manipulation targeted at decreasing pedestal growth rates and/or increasing pedestal shear rates. Fortunately, due to the complex parameter dependences of drift-type microinstabilities, there exist many prospective routes toward such manipulation, which should be vigorously pursued.

5.5. ITG particle pinch

Particle fueling and transport in the pedestal remain large open questions, with some estimates predicting that an edge particle pinch or pellet fueling may be required to fuel ITER [67, 68]. Here we discuss the potential role of ITG in pedestal particle transport. The two best candidates for pedestal particle transport are (1) KBM, which produces only diffusion, and (2) ITG (or other ion scale electrostatic modes), which is versatile enough to produce any combination of pinch and diffusion depending on the details of the parameter regime [69]. Interestingly, the ITG turbulence simulated in this work finds itself very near the point of balanced pinch and diffusion, as

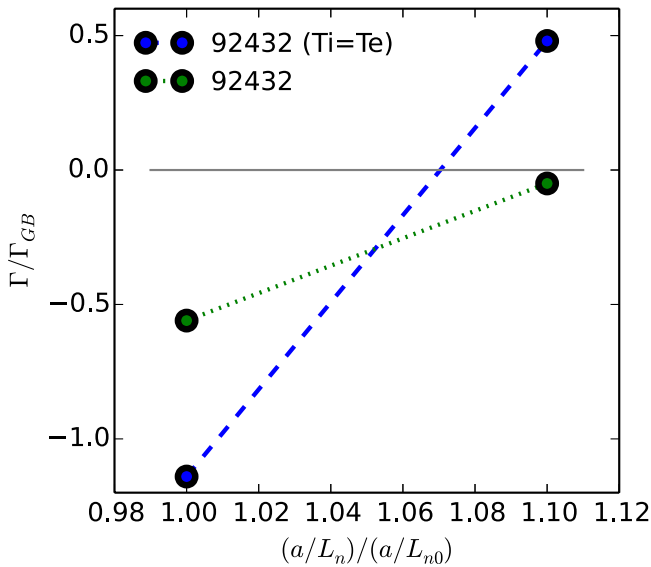


Figure 12. Particle flux from nonlinear global simulations of two JET-ILW (92432) simulations. The particle flux transitions from negative to zero or positive with a small increase in density gradient scale length, suggesting that the density pedestal reaches a state of balanced ITG pinch and diffusion.

shown in figure 12, which shows the particle transport from global nonlinear simulations over density gradient scans for two JET-ILW (92432) simulations: the nominal profiles with Be (see first column in figure 8) and the case with $T_i = T_e$ (see third column in figure 8). The scans shown in figure 12 entail a 10% increase in the density gradient scale length with a corresponding decrease in temperature gradients calculated to keep pressure fixed. Notably, with this moderate change, the transport transitions from negative to positive (or nearly so) for all both cases. This suggests that the ITG turbulence may be responsible for a particle pinch early in the ELM cycle and evolves to a state of balanced pinch and diffusion set by the properties of the ITG mode. More thorough analysis of these dynamics would rely on detailed examination of inter-ELM profile evolution in connection with edge modeling to estimate particle sources, which will be the topic of future work.

This ITG mechanism may be distinct to JET-ILW or may be operative in other pedestal scenarios. Since the other transport mechanisms (ETG and MTM) produce negligible particle transport, KBM and/or ITG may operate at low fluctuation levels (negligible for heat flux) and still mediate the density profile.

6. Summary and discussion

This paper describes a comparison between the gyrokinetic instabilities and resulting transport produced in two representative JET-C and JET-ILW pedestals (shots 92432 and 78697, respectively). The two discharges were selected to have high confinement at high current. They have similar values for many relevant parameters (β , I_p , B , etc) while retaining the distinguishing features of JET-C and JET-ILW, notably, decreased pedestal top temperature for JET-ILW. A comparison of the profiles and heating power reveals a stark qualitative difference

between the discharges: JET-ILW (92432) requires twice the heating power to sustain roughly half the temperature gradient of JET-C (78697). This points to the heat transport as a central feature of the dynamics underlying the limitations on the JET-ILW pedestal. This paper focuses on the relevant heat transport mechanisms, their important parameter dependences, and the interplay between these transport mechanisms and observed JET-ILW dynamics.

This work builds on [16] and expands on those results by, among other things, (1) directly comparing JET-ILW with JET-C pedestal transport, (2) using an experimentally diagnosed ion temperature profile, (3) employing global electromagnetic nonlinear gyrokinetic simulations, (4) identifying direct connections between MTMs and magnetic fluctuations in JET-C, and (5) identifying an ITG particle pinch. It reinforces the following emerging JET-ILW pedestal transport paradigm, which is proposed for further study. ILW conditions modify the density pedestal in ways that preferentially decrease the pedestal density gradient. This is attributable to some combination of direct effects of the metal wall on particle sources and the gas puffing necessary to mitigate W contamination. The modification to the density profile increases η_i and η_e , thereby producing more robust ITG and ETG instability which, in turn, limit the pedestal temperature and demand more heating power to achieve good pedestal performance. The decreased density gradient also decreases the flow shear rate, doubly enhancing the ion scale transport. The resulting decrease in pedestal temperature generally produces less favorable MHD stability and ultimately limits the pressure pedestal as well. This paradigm points to understanding and manipulating SOL and pedestal density as the key to optimizing pedestal performance for JET-ILW.

Nonlinear simulations of ETG and ITG transport for JET-ILW (92432), in combination with neoclassical ion heat flux, are compatible with carefully diagnosed inter-ELM heat losses. Global nonlinear simulations predict that ITG transport accounts for between $\sim 17\%$ – 47% of the inter-ELM transport depending on assumptions regarding impurity content. There are considerable uncertainties involved in diagnosing the ion temperature profile. Despite these uncertainties, the ILW equilibrium studied here clearly lies in a regime that, in comparison to standard pedestal scenarios, favors ITG turbulence. Consequently, these predictions of ITG turbulence should be taken seriously and be subject to continued examination via theory/simulation and experiment.

ITG and ETG turbulence are sensitive to the density gradient, impurities and ion dilution, and ITG is additionally sensitive to flow shear. Anomalous transport from these sources of temperature gradient driven turbulence could help explain several JET-ILW trends including: the strong limitation on accessible pedestal top temperatures; the observed degradation at high current/field (i.e. low ρ_*); and the increased confinement observed with impurity seeding. Scans of $E \times B$ shear predict the scaling $Q_i/Q_{GB} \propto \rho_*^{-1.7}$, finding close agreement with the scaling predicted by fundamental theory [40] and suggesting that, if a/L_{Ti} is fixed and above the ITG threshold, ITG turbulence will increase in impact as ρ_* decreases. Note that this scaling is only predicted for the ITG component of

the transport and not the total transport, which also includes substantial contributions from ETG. The presence of ITG also has potential implications for pedestal particle transport and pedestal density structure; nonlinear simulations scanning the density gradient find ITG to be in a regime of closely balanced pinch and diffusion, suggesting that it may be responsible for an inter-ELM particle pinch. To the extent that the JET-ILW pedestal is characterized by high η and low $E \times B$ shear, it lies in a unique parameter regime among present-day experiments that favors the excitation of ITG turbulence in the pedestal.

In contrast with JET-ILW (92432), our analysis suggests that JET-C (78697) is much more conventional in its composition of pedestal transport mechanisms, with heat transport dominated by a combination of ETG and MTM. ETG simulations predict substantial levels of transport in the pedestal (roughly half the inter-ELM power loss). MTMs are identified in global linear simulations and find close connections with washboard modes, which have long been observed in JET fluctuation data. A detailed comparison between MTM and magnetic spectrograms will be presented in a future paper. This mix of ETG and MTM transport appears to be quite common in the pedestal, and is similar to the findings of [18], which report similar analysis of two DIII-D discharges. Moreover, the MTMs observed here are similar to those reported in a gyrokinetic analysis of another JET-ILW shot [15]. In short, there is growing evidence that MTM is a common pedestal fluctuation across different operating scenarios on several machines.

The results described here are not in direct conflict with MHD-centric models of the pedestal like EPED. Such models may be consistent with the pre-ELM pressure pedestal structure and yet have limited predictive or explanatory power for scenarios like JET-ILW. For example, EPED uses pedestal top density as an input to the model. Consequently it is incapable of predicting or interpreting the observed JET-ILW changes in pedestal top density (note that a generalization of this framework has been developed for JET to get around such limitations [70]). Moreover, the question of the increased demand for heating power on JET-ILW is outside the scope of the EPED model. The main intersection of this work with EPED is analysis of KBM stability. In our analysis, KBM is found in local but not global simulations. The discrepancy can be attributed to the fact that the local mode structure is too broad radially to fit inside the narrow radial domain of the pedestal and thus would not be manifest in a global simulation. We note also, some remaining limitations in the global treatment, notably, the absence of the kink term and neglecting the vacuum solution beyond the separatrix. A possible indication of MHD activity is the clamping of the pressure profile midway through the ELM cycle. However, due to the underlying properties of MHD modes, such modes would be limited to constraining the pressure profile by preferentially producing transport in the most-weakly driven channel (particles). Consequently, KBM and other MHD modes can be eliminated as major heat transport mechanisms that constrain the JET-ILW pedestal temperature.

In summary, this work provides a framework for understanding the changes to pedestal transport that arise due to

the ILW and limit the pedestal temperature. This framework has the potential to inform pedestal optimization for JET-ILW and beyond and should be subject to ongoing examination by theory, computation, and experiment.

Acknowledgment

This research used resources of the National Energy Research Scientific Computing Center, a DOE Office of Science User Facility; the Texas Advanced Computing Center (TACC) at The University of Texas at Austin. We acknowledge the CINECA award under the ISCRA initiative, for the availability of high performance computing resources and support. We wish to acknowledge several members of the GENE development team, including F.S. Jenko, T. Görler, D. Told, and A. Bañón Navarro, for useful support and discussion. This work was supported by U.S. DOE Contract No. DE-FG02-04ER54742 and U.S. DOE Office of Fusion Energy Sciences Scientific Discovery through Advanced Computing (SciDAC) program under Award Number DE-SC0018429. This work has been carried out within the framework of the EUROfusion Consortium and has received funding from the Euratom research and training programme 2014–2018 under grant agreement No 633053. The views and opinions expressed herein do not necessarily reflect those of the European Commission.

Appendix. Numerical setup of gyrokinetic simulations

This work exploited several GENE modes of operation (local, global, linear, nonlinear, neoclassical), each with distinct numerical demands. Numerical details of the simulations are described in this appendix. All simulations were electromagnetic and employed Landau–Boltzmann collision operator with physical collision frequencies.

A.1. Global simulations

Global simulations use 320 radial grid points and span the domain shown in figure 1: $\rho_{\text{tor}} = 0.94\text{--}0.995$. This corresponds to approximately 50 sound gyroradii (with the gyro-radius calculated at the center of the radial domain). Dirichlet boundary conditions were enforced at the radial boundaries and transition regions were implemented (15% on each side) over which gradients are smoothly set to zero and Krook damping smoothly ramps up to set fluctuations to zero at the boundary. In nonlinear simulations, particle and heat sources (with coefficients of 0.05 in the normalized time units) were employed to fix the gradients at their background values.

Global simulations used 48 Fourier modes in k_y , with a minimum wavenumber $k_{y,\text{min}} = 0.041$ (i.e. k_y ranges from 0.0 to 1.9). Hyperdiffusion (6th order) was employed for k_y modes in order to damp high k_y ETG modes. The hyperdiffusion was tuned to eliminate high k_y electron modes while leaving the low k_y ion scale turbulence unaffected. Multiscale effects remain an open question in the pedestal and such simulations should be a high future priority to determine what, if any,

affects of cross-scale coupling are important. In the parallel z , parallel velocity $v_{||}$, and magnetic moment μ (i.e. squared perpendicular velocity), (64, 64, 24) grid points were used, respectively. The parallel domain was from $-\pi$ to π (poloidal angle), the parallel velocity domain was -4 to 4 (normalized to $\sqrt{T_e/m_i}$), and the μ coordinate ranges from 0 to 11 (normalized to T_e/B_0).

Numerical instabilities were encountered in some non-linear global simulations, often after a substantial period of nonlinear saturation. In such cases β was slightly reduced and the simulations were extended successfully with no instability. For the simulations of shot 92432, minor reductions succeeded in extending the duration of the simulations and a 40% reduction appeared to eliminate the numerical instability. These reductions in β had no effect on turbulence levels since the ITG modes of interest are insensitive to β in this regime (see figure 6). The simulations of shot 78697 were more challenging. Minor reductions (a few ten percent) of β were not sufficient to eliminate the numerical instability. Larger reductions in β (>50%) eliminated numerical instabilities but placed the system in the regime of spurious electron drift modes discussed in the context of figure 6. Simulations with beta values close to the ideal ballooning threshold tend to be very challenging and will be published elsewhere, highlighting the capabilities of some of GENE's newly developed numerical schemes for treating high-beta regimes.

Convergence tests in all coordinates were conducted by comparing simulation results through the initial saturation period and ensuring minimal changes with increases in resolution.

A.2. Flux tube ETG simulations

Single scale ETG simulations with adiabatic ions were conducted for both JET-C and JET-ILW using the local flux tube approximation. 240, 36, 8 grid points in the $z, v_{||}, \mu$ coordinates, with a radial wavenumber grid resolving from $k_{x,\min}\rho_s = 2.6$ to $k_{x,\max}\rho_s = 164$ and a wavenumber grid in the y coordinate resolving from $k_{y,\min}\rho_s = 5$ to $k_{y,\max}\rho_s = 235$. The parallel domain was from $-\pi$ to π (poloidal angle), the parallel velocity domain was -3 to 3 , and the μ coordinate ranges from 0 to 9. These simulations relied on convergence tests carried out in the course of earlier work [15].

A.3. Local linear simulations

Local linear simulations used 96, 48, 16 grid points in the $z, v_{||}, \mu$ coordinates along with 13 k_x modes. The parallel grid resolution was increased substantially ($\gtrsim 240$) for ETG simulations. The parallel domain was from $-\pi$ to π (poloidal angle), the parallel velocity domain was -3 to 3 , and the μ coordinate ranges from 0 to 9.

A.4. Neoclassical simulations

Local neoclassical simulations used 48, 96, 48 grid points in the $z, v_{||}, \mu$ coordinates. The parallel domain was from $-\pi$ to

π (poloidal angle), the parallel velocity domain was -3 to 3 , and the μ coordinate ranges from 0 to 9.

ORCID iDs

D.R. Hatch  <https://orcid.org/0000-0002-1625-4385>

C.F. Maggi  <https://orcid.org/0000-0001-7208-2613>

C. Perez von Thun  <https://orcid.org/0000-0002-1166-2179>

References

- [1] Philipps V., Mertens Ph., Matthews G. and Maier H. 2010 Overview of the JET ITER-like wall project *Fusion Eng. Des.* **85** 1581–6 (*Proc. of the 9th Int. Symp. on Fusion Nuclear Technology*)
- [2] Matthews G.F. et al 2011 JET ITER-like wall overview and experimental programme *Phys. Scr.* **2011** 014001
- [3] Wagner F. et al 1982 Regime of improved confinement and high beta in neutral-beam-heated divertor discharges of the ASDEX tokamak *Phys. Rev. Lett.* **49** 1408–12
- [4] Giroud C. et al 2013 Impact of nitrogen seeding on confinement and power load control of a high-triangularity JET elmy H-mode plasma with a metal wall *Nucl. Fusion* **53** 113025
- [5] Beurskens M.N.A. et al 2013 The effect of a metal wall on confinement in JET and ASDEX Upgrade *Plasma Phys. Control. Fusion* **55** 124043
- [6] Joffrin E. et al 2014 First scenario development with the JET new ITER-like wall *Nucl. Fusion* **54** 013011
- [7] Leyland M. et al 2015 The H-mode pedestal structure and its role on confinement in JET with a carbon and metal wall *Nucl. Fusion* **55** 013019
- [8] Maggi C. et al 2015 Pedestal confinement and stability in JET-ILW elmy H-modes *Nucl. Fusion* **55** 113031
- [9] Giroud C. et al 2015 Progress at JET in integrating ITER-relevant core and edge plasmas within the constraints of an ITER-like wall *Plasma Phys. Control. Fusion* **57** 035004
- [10] Kim H.-T., Romanelli M., Voitikhovitch I., Koskela T., Conboy J., Giroud C., Maddison G., Joffrin E. and JET Contributors 2015 Comparative analysis of core heat transport of JET high density H-mode plasmas in carbon wall and ITER-like wall *Plasma Phys. Control. Fusion* **57** 065002
- [11] Nunes I. and the JET Contributors 2016 Plasma confinement at JET *Plasma Phys. Control. Fusion* **58** 014034
- [12] Beurskens M.N.A. et al 2014 Global and pedestal confinement in JET with a Be/W metallic wall *Nucl. Fusion* **54** 043001
- [13] Jenko F., Dorland W., Kotschenreuther M. and Rogers B. 2000 Electron temperature gradient driven turbulence *Phys. Plasmas* **7** 1904
- [14] Görler T., Lapillonne X., Brunner S., Dannert T., Jenko F., Merz F. and Told D. 2011 The global version of the gyrokinetic turbulence code GENE *J. Comput. Phys.* **230** 7053–71
- [15] Hatch D.R., Kotschenreuther M., Mahajan S., Valanju P., Jenko F., Told D., Görler T. and Saarelma S. 2016 Microtearing turbulence limiting the JET-ILW pedestal *Nucl. Fusion* **56** 104003
- [16] Hatch D.R., Kotschenreuther M., Mahajan S., Valanju P. and Liu X. 2017 A gyrokinetic perspective on the JET-ILW pedestal *Nucl. Fusion* **57** 036020
- [17] Kotschenreuther M., Hatch D.R., Mahajan S., Valanju P., Zheng L. and Liu X. 2017 Pedestal transport in H-mode plasmas for fusion gain *Nucl. Fusion* **57** 064001

- [18] Kotschenreuther M. Gyrokinetic analysis and simulation of pedestals, to identify the culprits for energy losses using ‘fingerprints’ *Nucl. Fusion* (<https://doi.org/10.1088/1741-4326/ab1fa2>)
- [19] Dickinson D., Roach C.M., Saarelma S., Scannell R., Kirk A. and Wilson H.R. 2012 Kinetic instabilities that limit β in the edge of a tokamak plasma: a picture of an H-mode pedestal *Phys. Rev. Lett.* **108** 135002
- [20] Saarelma S., Beurskens M., Dickinson D., Frassinetti L., Leyland M., Roach C. and EFDA-JET Contributors 2013 Mhd and gyro-kinetic stability of JET pedestals *Nucl. Fusion* **53** 123012
- [21] Hillesheim J.C., Dickinson D., Roach C.M., Saarelma S., Scannell R., Kirk A., Crocker N.A., Peebles W.A., Meyer H. and The MAST Team 2016 Intermediate- k density and magnetic field fluctuations during inter-ELM pedestal evolution in mast *Plasma Phys. Control. Fusion* **58** 014020
- [22] Wolfrum E. *et al* 2017 Impact of wall materials and seeding gases on the pedestal and on core plasma performance *Nucl. Mater. Energy* **12** 18–27
- [23] Stefanikova E. *et al* 2018 Effect of the relative shift between the electron density and temperature pedestal position on the pedestal stability in JET-ILW and comparison with JET-C *Nucl. Fusion* **58** 056010
- [24] Snyder P., Groebner R., Leonard A., Osborne T. and Wilson H. 2009 Development and validation of a predictive model for the pedestal height *Phys. Plasmas* **16** 056118
- [25] Snyder P. *et al* 2009 Pedestal stability comparison and ITER pedestal prediction *Nucl. Fusion* **49** 085035
- [26] Bowman C. *et al* 2018 Pedestal evolution physics in low triangularity JET tokamak discharges with ITER-like wall *Nucl. Fusion* **58** 016021
- [27] Aiba N. *et al* 2017 Numerical analysis of elm stability with rotation and ion diamagnetic drift effects in JET *Nucl. Fusion* **57** 126001
- [28] Aiba N. *et al* 2018 Analysis of ELM stability with extended MHD models in JET, JT-60U and future JT-60SA tokamak plasmas *Plasma Phys. Control. Fusion* **60** 014032
- [29] Giroud C. *et al* 2018 Optimisation of JET-DT and iter operation by developing an understanding of the role of low- z impurity on the H-mode pedestal *IAEA Fusion Energy Conf. (Gandhinagar, India, 22–27 October 2018)* EX/3-4 (<https://www.iaea.org/events/fec-2018>)
- [30] Dunne M.G. *et al* 2017 The role of the density profile in the ASDEX-Upgrade pedestal structure *Plasma Phys. Control. Fusion* **59** 014017
- [31] Angioni C., Candy J., Fable E., Maslov M., Peeters A.G., Waltz R.E. and Weisen H. 2009 Particle pinch and collisionality in gyrokinetic simulations of tokamak plasma turbulence *Phys. Plasmas* **16** 060702
- [32] Callen J.D., Groebner R.J., Osborne T.H., Canik J.M., Owen L.W., Pankin A.Y., Rafiq T., Rognlien T.D. and Stacey W.M. 2010 Analysis of pedestal plasma transport *Nucl. Fusion* **50** 064004
- [33] Horton L. *et al* 2005 Characterization of the H-mode edge barrier at ASDEX Upgrade *Nucl. Fusion* **45** 856
- [34] Chankin A.V. *et al* 2006 Solps modelling of ASDEX Upgrade H-mode plasma *Plasma Phys. Control. Fusion* **48** 839
- [35] Perez C.P. *et al* 2003 Washboard modes as ELM-related events in JET *Plasma Phys. Control. Fusion* **46** 61
- [36] Diallo A. *et al* 2014 Observation of edge instability limiting the pedestal growth in tokamak plasmas *Phys. Rev. Lett.* **112** 115001
- [37] Diallo A., Groebner R.J., Rhodes T.L., Battaglia D.J., Smith D.R., Osborne T.H., Canik J.M., Guttenfelder W. and Snyder P.B. 2015 Correlations between quasi-coherent fluctuations and the pedestal evolution during the inter-edge localized modes phase on DIII-D *Phys. Plasmas* **22** 056111
- [38] Laggner F.M. *et al* 2016 High frequency magnetic fluctuations correlated with the inter-ELM pedestal evolution in ASDEX Upgrade *Plasma Phys. Control. Fusion* **58** 065005
- [39] Maggi C. *et al* 2017 Studies of the pedestal structure and inter-ELM pedestal evolution in JET with the ITER-like wall *Nucl. Fusion* **57** 116012
- [40] Hatch D.R., Hazeltine R.D., Kotschenreuther M.K. and Mahajan S.M. 2018 Flow shear suppression of pedestal ion temperature gradient turbulence—a first principles theoretical framework *Plasma Phys. Control. Fusion* **60** 084003
- [41] Bokshi A., Dickinson D., Roach C.M. and Wilson H.R. 2016 The response of toroidal drift modes to profile evolution: a model for small-ELMs in tokamak plasmas? *Plasma Phys. Control. Fusion* **58** 075011
- [42] Saarelma S., Jrvinen A., Beurskens M., Challis C., Frassinetti L., Giroud C., Groth M., Leyland M., Maggi C. and Simpson J. 2015 The effects of impurities and core pressure on pedestal stability in joint european torus (JET) *Phys. Plasmas* **22** 056115
- [43] Kim H.-T. *et al* 2018 High fusion performance at high T_i/T_e in JET-ILW baseline plasmas with high NBI heating power and low gas puffing *Nucl. Fusion* **58** 036020
- [44] Field A.R., Frassinetti L., Maggi C., Saarelma S. and JET Contributors 2018 Inter-ELM power losses and their dependence on pedestal parameters in JET-C and ITER-like wall H-mode plasmas *Proc. of the 2018 EPS Conf. (Prague, Czech Republic, 2–6 July 2018)* (<https://eps2018.eli-beams.eu/en/>)
- [45] Haskey S.R. *et al* 2018 Active spectroscopy measurements of the deuterium temperature, rotation, and density from the core to scrape off layer on the DIII-D tokamak (invited) *Rev. Sci. Instrum.* **89** 10D110
- [46] Haskey S.R. *et al* 2018 Main ion and impurity edge profile evolution across the L- to H-mode transition on DIII-D *Plasma Phys. Control. Fusion* **60** 105001
- [47] McMillan B.F., Lapillonne X., Brunner S., Villard L., Jolliet S., Bottino A., Görler T. and Jenko F. 2010 System size effects on gyrokinetic turbulence *Phys. Rev. Lett.* **105**
- [48] Beer M.A., Cowley S.C. and Hammett G.W. 1995 Field aligned coordinates for nonlinear simulations of tokamak turbulence *Phys. Plasmas* **2** 687–700
- [49] Wang E., Xu X., Candy J., Groebner R., Snyder P., Chen Y., Parker S., Wan W., Lu G. and Dong J. 2012 Linear gyrokinetic analysis of a DIII-D H-mode pedestal near the ideal ballooning threshold *Nucl. Fusion* **52** 103015
- [50] Hatch D., Told D., Jenko F., Doerk H., Dunne M., Wolfrum E., Viezzer E., Pueschel M. and The ASDEX Upgrade Team 2015 Gyrokinetic study of ASDEX Upgrade inter-ELM pedestal profile evolution *Nucl. Fusion* **55** 063028
- [51] Canik J., Guttenfelder W., Maingi R., Osborne T., Kubota S., Ren Y., Bell R., Kugel H., LeBlanc B. and Souhkanovskii V. 2013 Edge microstability of NSTX plasmas without and with lithium-coated plasma-facing components *Nucl. Fusion* **53** 113016
- [52] Saarelma S., Martin-Collar J., Dickinson D., McMillan B.F., Roach C.M., MAST Team and The JET Contributors 2017 Non-local effects on pedestal kinetic ballooning mode stability *Plasma Phys. Control. Fusion* **59** 064001
- [53] Doerk H. 2013 *Gyrokinetic Simulation of Microtearing Turbulence*, Dissertation University of Ulm (<https://doi.org/10.18725/OPARU-2600>)
- [54] Görler T. *et al* 2011 Flux- and gradient-driven global gyrokinetic simulation of tokamak turbulence *Phys. Plasmas* **18** 056103
- [55] Told D., Jenko F., Xanthopoulos P., Horton L.D. and Wolfrum E. 2008 Gyrokinetic microinstabilities in ASDEX Upgrade edge plasmas *Phys. Plasmas* **15** 102306
- [56] Jenko F., Told D., Xanthopoulos P., Merz F. and Horton L.D. 2009 Gyrokinetic turbulence under near-separatrix or nonaxisymmetric conditions *Phys. Plasmas* **16** 055901

- [57] Reshko M., Roach C.M. and The MAST Team 2008 Effects of impurities on electron temperature gradient modes *Plasma Phys. Control. Fusion* **50** 115002
- [58] Landreman M. and Ernst D.R. 2012 Local and global fokkerplanck neoclassical calculations showing flow and bootstrap current modification in a pedestal *Plasma Phys. Control. Fusion* **54** 115006
- [59] Viezzer E. *et al* 2013 High-accuracy characterization of the edge radial electric field at ASDEX Upgrade *Nucl. Fusion* **53** 053005
- [60] Battaglia D.J., Burrell K.H., Chang C.S., Ku S., deGrassie J.S. and Grierson B.A. 2014 Kinetic neoclassical transport in the H-mode pedestal *Phys. Plasmas* **21** 072508
- [61] Viezzer E. *et al* 2017 Investigation of inter-ELM ion heat transport in the H-mode pedestal of ASDEX Upgrade plasmas *Nucl. Fusion* **57** 022020
- [62] Zhang Y.Z. and Mahajan S.M. 1992 Edge turbulence scaling with shear flow *Phys. Fluids B* **4** 1385–7
- [63] Zhang Y.Z. and Mahajan S.M. 1993 Correlation theory of a two-dimensional plasma turbulence with shear flow *Phys. Fluids B* **5** 2000–20
- [64] Frassinetti L. *et al* 2017 Dimensionless scalings of confinement, heat transport and pedestal stability in JET-ILW and comparison with JET-C *Plasma Phys. Control. Fusion* **59** 014014
- [65] Nunes I. *et al* 2013 Confinement and edge studies towards low ρ^* and ν^* at JET *Nucl. Fusion* **53** 073020
- [66] Chang C. *et al* 2017 Gyrokinetic projection of the divertor heat-flux width from present tokamaks to ITER *Nucl. Fusion* **57** 116023
- [67] Kukushkin A., Pacher H., Pacher G., Janeschitz G., Coster D., Loarte A. and Reiter D. 2003 Scaling laws for edge plasma parameters in iter from two-dimensional edge modelling *Nucl. Fusion* **43** 716
- [68] Garzotti L. *et al* 2012 Simulations of density profiles, pellet fuelling and density control in ITER *Nucl. Fusion* **52** 013002
- [69] Angioni C., Camenen Y., Casson F., Fable E., McDermott R., Peeters A. and Rice J. 2012 Off-diagonal particle and toroidal momentum transport: a survey of experimental, theoretical and modelling aspects *Nucl. Fusion* **52** 114003
- [70] Saarelma S., Challis C.D., Garzotti L., Frassinetti L., Maggi C.F., Romanelli M., Stokes C. and JET Contributors 2018 Integrated modelling of H-mode pedestal and confinement in JET-ILW *Plasma Phys. Control. Fusion* **60** 014042
- [71] Litaudon X. *et al* 2017 *Nucl. Fusion* **57** 102001